Chemical Geology 255 (2008) 283–293

Contents lists available at ScienceDirect

Chemical Geology

journal homepage: www.elsevier.com/locate/chemgeo

# Rutile solubility in $H_2O$, $H_2O$–$SiO_2$, and $H_2O$–$NaAlSi_3O_8$ fluids at 0.7–2.0 GPa and 700–1000 °C: Implications for mobility of nominally insoluble elements

Angelo Antignano [1], Craig E. Manning *

*Department of Earth and Space Sciences, University of California Los Angeles, Los Angeles, CA, 90095-1567, USA*

ARTICLE INFO

*Article history:*
Received 27 March 2008
Received in revised form 1 July 2008
Accepted 2 July 2008

Editor: J. Fein

*Keywords:*
Rutile solubility
High-field-strength elements
Ti mobility
Fluid flow

ABSTRACT

The solubility of rutile was measured in $H_2O$, $H_2O$–$SiO_2$ and $H_2O$–$NaAlSi_3O_8$ fluids at 700–1000 °C, 0.7–2.0 GPa, in a piston-cylinder apparatus. Solubility was determined by weight loss using a double-capsule method. Rutile solubility in pure $H_2O$ shows isothermal increase with pressure ($P$), isobaric increase with temperature ($T$), and is low at all conditions investigated (6–118 ppm Ti). Rutile solubility in $H_2O$ is given by $\log c^{\circ}_{Ti} = 6.173 - 5425/T + 178.4P/T$, where $c^{\circ}_{Ti}$ is Ti concentration in ppm, $T$ is in K, and $P$ in GPa. This leads to thermodynamic properties of the reaction rutile = $TiO_{2,aq}$ of $\Delta S^{\circ}_r = 28.6$ J/mol K, $\Delta H^{\circ}_r = 104$ kJ/mol, and $\Delta V^{\circ}_r = -3.4$ cm$^3$/mol. At 800 °C and 1 GPa, addition of $SiO_2$ (up to quartz saturation) did not change rutile solubility relative to that in pure $H_2O$. Determination of rutile solubility in $H_2O$–$NaAlSi_3O_8$ fluids was complicated by incongruent dissolution of albite to paragonite or corundum + fluid; however, fluid compositions could be estimated within narrow limits using a mass-balance scheme. The solubility of rutile increases linearly with dissolved Na–Al silicate at fixed $P$ and $T$, as described by $c_{Ti} = c^{\circ}_{Ti} + Bw_s$ where $c_{Ti}$ is ppm Ti, $w_s$ is wt.% dissolved silicate and $B$ is given by $\log B\ 6.512 - 1.665P - 6224/T + 2215P/T$, with $T$ and $P$ again in K and GPa.

The results help explain discrepancies among previous studies of rutile solubility in $H_2O$ at similar $P$ and $T$. The new data agree within error with those of Tropper and Manning [Tropper, P., Manning, C.E., 2005. Very low solubility of rutile in $H_2O$ at high pressure and temperature, and its implications for Ti mobility in subduction zones. American Mineralogist 90, 502–505.], but give lower solubility than earlier piston-cylinder-based determinations due to suppression of new crystal growth in the present experiments. However, the new data yield higher solubilities than are predicted from a hydrothermal diamond-anvil study, probably because of our longer run times and more complete equilibration. Combination of predicted Ti concentrations in melt-saturated $H_2O$ with $H_2O$-saturated albite melts suggests that the melt–vapor partition coefficient for Ti is constant at 9.5 ± 1.5 from 700 to 900 °C at 1 GPa and rutile saturation, implying that an $H_2O$-rich magmatic vapor phase can transport significant Ti in mid- to deep-crustal settings. Because crustal and mantle fluids will contain alkalis, Al and Si, the results in $H_2O$–$NaAlSi_3O_8$ fluids provide a better foundation for modeling high-$P$ metasomatic processes than pure $H_2O$ values. The strong increase in rutile solubility with dissolved Na–Al silicate suggests that complexing with these constituents promotes Ti mobility and transport during fluid–rock interaction in the lower crust and upper mantle.



## 1. Introduction

Rutile ($TiO_2$) is an important accessory mineral in igneous, metamorphic and sedimentary rocks. It is a key metamorphic index phase (e.g., Ernst and Liu, 1998), and its common occurrence makes it useful for net-transfer and exchange thermobarometry (e.g., Bohlen et al., 1983; Manning and Bohlen, 1991; Zack et al., 2004a; Watson and Harrison, 2005; Watson et al., 2006; Zack and Luvizottow, 2006; Tomkins et al., 2007; Tropper and Manning, in press) and U–Pb geochronometry (Corfu and Andrews, 1986; Mezger et al., 1989, 1991). Because it readily accommodates high-field-strength elements (HFSE), rutile has proven effective as a monitor of geochemical processes such as magma evolution, subduction-zone metasomatism, and element cycling (e.g., Ryerson and Watson, 1987; Ayers and Watson, 1991, 1993; Brenan et al., 1994; Stalder et al., 1998; Foley et al., 2000; Rudnick et al., 2000; Zack et al., 2002; Klemme et al., 2005). Moreover, rutile's high durability in diagenetic contexts makes it a sensitive record of sedimentary provenance (Force, 1980; Zack et al., 2004b; Triebold et al., 2007).

Essential to understanding the role of rutile in such a wide range of geochemical processes is knowledge of its behavior in the presence of geologic fluids. It is often assumed that rutile has very low solubility in aqueous fluids in most settings. This has been based in part on low Ti concentrations of surface and diagenetic waters (van Baalen, 1993), on experimental studies which return low rutile solubility in $H_2O$-rich solutions at moderate pressure ($P$) and temperature ($T$) (Schuiling and

* Corresponding author.
*E-mail addresses:* angelo.antignano@exxonmobil.com (A. Antignano), manning@ess.ucla.edu (C.E. Manning).
[1] Current address: Exxon Mobil Corporation, PO Box 4778, Houston, Texas, 77210-4770, USA.

0009-2541/$ – see front matter © 2008 Elsevier B.V. All rights reserved.
doi:10.1016/j.chemgeo.2008.07.001

Vink, 1967; Barsukova et al., 1979; Agapova et al., 1989), and on the observation that rutile is a common residual mineral during hydrothermal alteration (e.g., Marsh, 1979; Czamanske et al., 1981; Force, 1991). The low apparent mobility of Ti has led to models in which conservation of this element aids identification of protolith or tectonic setting of formation of metaigneous rocks (e.g., Pearce and Cann, 1971, 1973; Floyd and Winchester, 1975, 1978; Pearce and Norrey, 1979). However, under appropriate conditions rutile may exhibit elevated solubility, which can lead to significant Ti mobility (van Baalen, 1993; Jiang et al., 2005). In particular, some high-*P* metamorphic environments exhibit evidence for elevated rutile solubility in the form of rutile daughter crystals in fluid inclusions, rutile in veins, and shifts in whole-rock $TiO_2$ concentration (e.g., Sorensen and Grossman, 1989; Philippot and Selverstone, 1991; Selverstone et al., 1991; Gao and Klemd, 2001; Rubatto and Hermann, 2003; Gao et al., 2007). A possible explanation would be large increases in rutile solubility in $H_2O$ with rising *P* and *T*; however, experimental studies yield inconsistent results. Early data supported high solubility (Ayers and Watson, 1993). More recent investigations suggest lower values, but differ as to the magnitude of the disparity (Audétat and Keppler, 2005; Tropper and Manning, 2005). Alternative scenarios might be extreme pH shifts toward acidic or basic conditions (van Baalen, 1993), or high concentrations of a complexing element such as fluorine (e.g., Barsukova et al., 1979; Gieré, 1990); however, it is unlikely that such explanations can account for all occurrences. Thus, the origin of enhanced Ti mobility – evidently, a common feature of metasomatism in high-*P* terranes – remains uncertain.

To resolve this problem, we conducted experiments on the solubility of rutile in three types of geologic fluids at high *P* and *T*. The first set of experiments involved pure $H_2O$, and was aimed at addressing the discrepancies in previous work and at extending measurements to conditions more appropriate for metamorphic and magmatic systems. We also investigated rutile solubility in $H_2O$–$SiO_2$ and $H_2O$–albite fluids. These experiments were motivated by the recent recognition that nominally insoluble elements may have their solubility enhanced via complexing with aqueous $SiO_2$ or Na–Al-silicate clusters or polymers (Manning, 2004, 2007). The new results provide constraints on Ti mobility in geologic settings and HFSE cycling in the Earth.

## 2. Methods

### 2.1. Experimental

The experiments utilized the same pure synthetic rutile as in the study of Tropper and Manning (2005). Methods were similar to those of Antignano and Manning (2008). Briefly, small single-crystal chips of rutile were smoothed with emery paper, cleaned ultrasonically, and then dried at 400 °C. We used a double-capsule arrangement, in which a single crystal was loaded into a protective 1.6 mm OD × 6 mm Pt tube that was then lightly crimped. This inner capsule was loaded into a 3.5 mm OD Pt tube with ultrapure $H_2O$ and, in some cases, powdered high-purity natural quartz (Bahia Brazil; Manning, 1994) or albite (Amelia courthouse, 0.29 wt.% $K_2O$, Kracek and Neuvonen, 1952). The outer capsule was sealed by arc-welding and placed in a 115 °C oven for 1 h to check for leakage; incompletely sealed capsules were identified by any weight loss and were not used. The double-capsule geometry provides for containment of crystals if they break, segregates crystals from most of the fluid to minimize back-reaction during quench, and reduces temperature gradients in the charge during the run.

The experiments were conducted in a piston-cylinder apparatus using 2.54-cm NaCl–graphite assemblies (Manning, 1994; Manning and Boettcher, 1994; Antignano and Manning, 2008). Run conditions of 0.7–2.0 GPa and 700–1000 °C were attained using the piston-out method. Temperature was controlled with calibrated Pt–$Pt_{90}Rh_{10}$ thermocouples, with no correction for the effect of pressure on emf, and an estimated accuracy of ±3 °C. Pressure was monitored with a Heise gauge and held to within 200 bars of the target gauge pressure. Rapid quenching to <50 °C within 1 min was achieved by cutting the power to the apparatus (Manning and Boettcher, 1994).

Rutile solubilities were determined from the loss in weight of the crystals. After experiments in pure $H_2O$ and $H_2O$–$SiO_2$, rutile grains were extracted and placed in ultrapure $H_2O$ and subjected to an ultrasonic bath, dried at 115 °C, and then weighed. In experiments in the system $H_2O$–albite, quench material typically adhered to the rutile grains even after ultrasonic treatment. In these cases, the rutile grain was placed in an HF bath for 15 s at room *T*, which was sufficient to loosen or dissolve the silicate quench from the crystal surface. Control tests showed that there was no detectible weight change of quench-free rutile subjected to identical treatment. Following the acid bath, the grains were rinsed with ultrapure $H_2O$, dried at 115 °C and weighed. Any experiment in which the rutile crystal broke was rejected.

Weights of rutile crystals were determined with a Mettler UMX2 ultramicrobalance ($1\sigma$=0.2 μg). Albite, quartz and $H_2O$ weights were determined with a Mettler M3 microbalance ($1\sigma$=2 μg). All run products were studied in detail by optical microscopy; materials from selected experiments were mounted and characterized by scanning electron microscope (SEM).

### 2.2. Concentration of dissolved silicate in $H_2O$–albite experiments

Experiments conducted with albite were complicated by the incongruent dissolution of this phase (Currie, 1968; Anderson and Burnham, 1983; Stalder et al., 2000; Shmulovich et al., 2001). In all $H_2O$–albite experiments, minor amounts of residual paragonite (700 °C) or corundum (800 and 900 °C) were observed in the run products. The residual phases were too finely dispersed and low in abundance to collect and weigh. Dissolved silicate concentrations in experimental fluids were therefore shifted to a small but immeasurable extent from the weight of the albite loaded into the capsules.

Although the dissolved Na–Al-silicate composition could not be measured, it can be constrained within narrow limits from the ratio of Na molality ($m_{Na}$) to Al molality ($m_{Al}$). If the residual phase is corundum ($Al_2O_3$), mass balance requires that

$$\frac{m_{Na}}{m_{Al}} = \frac{n_{ab}}{n_{ab} - 2n_{co}} \tag{1}$$

where $n_{ab}$ and $n_{co}$ respectively denote moles of albite added to an experiment and moles of corundum remaining. Rearranging and converting to mass units gives

$$w_{co} = w_{ab}\left(\frac{m_{Na}/m_{Al} - 1}{2m_{Na}/m_{Al}}\right)\left(\frac{\overline{w}_{co}}{\overline{w}_{ab}}\right) \tag{2}$$

where $w_{ab}$ and $w_{co}$ are respectively the masses of albite added and corundum remaining, and $\overline{w}$ denotes the molecular weight of the subscripted compound. Similarly, if paragonite (pg, $NaAl_3Si_3O_{10}(OH)_2$) is the incongruent dissolution product, then the mass mass-balance equation is:

$$\frac{m_{Na}}{m_{Al}} = \frac{n_{ab} - n_{pg}}{n_{ab} - 3n_{pg}} \tag{3}$$

which leads to

$$w_{pg} = w_{ab}\left(\frac{m_{Na}/m_{Al} - 1}{3m_{Na}/m_{Al} - 1}\right)\left(\frac{\overline{w}_{pg}}{\overline{w}_{ab}}\right). \tag{4}$$

The total concentration of dissolved Na–Al silicate, $w_s$, can then be calculated from

$$w_s = \frac{w_{ab} - w_{rm}}{w_{H_2O} + w_{ab} - w_{rm}} \tag{5}$$

where $w_{rm}$ is the weight of the residual mineral from Eq. (2) or (4) (i.e., $w_{co}$ or $w_{pg}$) and $w_{H_2O}$ is the weight of $H_2O$ in the experiment.

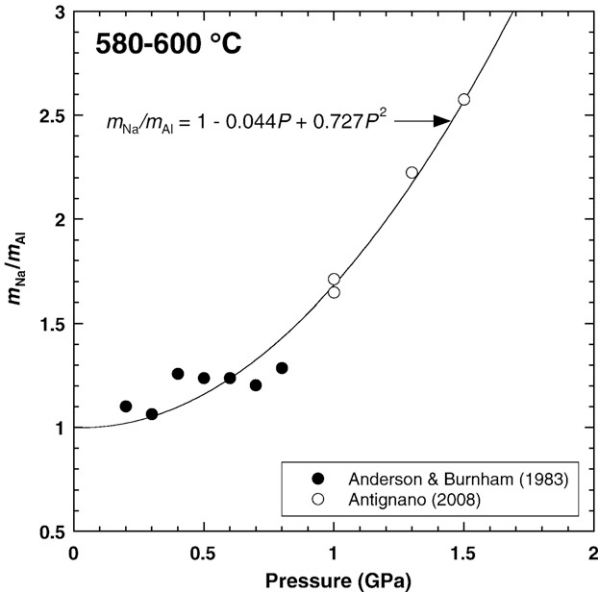


**Fig. 1.** Variation in the ratio of Na molality to Al molality with pressure in albite + paragonite + $H_2O$ and albite + corundum + $H_2O$ experiments at 580–600 °C. The derived fit equation was used to compute this ratio in experiments of the present study, but at higher *T* (see text).

The $m_{Na}/m_{Al}$ ratio at each experimental *P*, *T* and bulk composition is unknown; however, it can be tightly constrained. The minimum value of the ratio is one, corresponding to congruent dissolution (the ratio cannot be less than one because the residual phases are more aluminous than albite). The maximum value can be calculated from studies of albite solubility in $H_2O$ at high *P* and *T*. Anderson and Burnham (1983) found that albite dissolves incongruently yielding residual paragonite at 600 and 700 °C, 0.2–0.8 GPa, and that $m_{Na}/m_{Al}$ was constant at 1.2 ± 0.1 (1$\sigma$) in fluids coexisting with albite + paragonite. Antignano (2008) extended these results to higher *P* at 580 °C, and found that paragonite remained the incongruent dissolution product, but $m_{Na}/m_{Al}$ increased with increasing *P* (Fig. 1). The combined data sets constrain the isothermal dependence of $m_{Na}/m_{Al}$ on *P* at 580–600 °C via the fit equation

$$\frac{m_{Na}}{m_{Al}} = 1 - 0.044P + 0.727P^2 \tag{6}$$

where *P* is in GPa (Fig. 1). The value of $m_{Na}/m_{Al}$ calculated from Eq. (6) at a given *P* is a maximum for our experimental solutions because, with increasing *T*, there is a strong isobaric increase in the solubility of Al relative to that of Na (Tropper and Manning, 2007; Antignano, 2008).

Table 1 gives the range in dissolved silicate content derived from the approach described above. On average, the adjustment to the dissolved silicate was −5 ± 5% of the nominal value; the maximum was −7.5 ± 7.5% (Table 1).

### 2.3. Solubility calculation and error propagation

Because the investigated solutions included $H_2O$ and more complex solutions, rutile solubility ($c_{Ti}$) is reported in parts per million Ti by weight, as determined from

$$c_{Ti} = \frac{0.5995(\Delta w_{ru})}{(w_{H_2O} + w_s + \Delta w_{ru})} \times 10^6 \tag{7}$$

where $\Delta w_{ru}$ is the weight change of the rutile crystal and the factor 0.5995 is the mass fraction Ti in $TiO_2$. For experiments in $H_2O$ and $H_2O$-$SiO_2$ fluids, the standard deviation in $c_{Ti}$, $\sigma_c$, was derived by propagation of weighing errors:

$$\sigma_c = \left[ (c_{Ti})^2 \left( \frac{2\sigma_{ru}^2}{(\Delta w_{ru})^2} + \frac{2\sigma_{ru}^2 + \sigma_{H_2O}^2 + \sigma_s^2}{(w_{H_2O} + w_s + \Delta w_{ru})^2} \right) \right]^{\frac{1}{2}} \tag{8}$$

where $\sigma_{ru} = 2 \times 10^{-4}$ mg and $\sigma_{H_2O} = 2 \times 10^{-3}$ mg, as determined for the microbalances used to weigh each material. In rutile–$H_2O$–$SiO_2$ experiments, $\sigma_s = 2 \times 10^{-3}$ mg in the one experiment in which quartz dissolved completely (RQ-1, Table 1), as determined by propagation of weighing errors. Where quartz remained, $SiO_2$ concentration was taken from Manning (1994), with corresponding $\sigma_s = 4 \times 10^{-2}$ mg. In rutile–$H_2O$–albite experiments, the calculated error in $c_{Ti}$ must account for the fact that the concentration of dissolved silicate could only be limited between a minimum and maximum value. This translates to a range in $c_{Ti}$ (Eq. (7)). Assuming equal probability of any value within this range, $\sigma_c$ for rutile–$H_2O$–albite experiments is given by a modified form of Eq. (8):

$$\sigma_c = \left[ (c_{Ti})^2 \left( \frac{2\sigma_{ru}^2}{(\Delta w_{ru})^2} + \frac{2\sigma_{ru}^2 + \sigma_{H_2O}^2 + \sigma_s^2}{(w_{H_2O} + w_s + \Delta w_{ru})^2} \right) \right]^{\frac{1}{2}} + \left[ \frac{(c_{Ti}^{max} - c_{Ti}^{min})^2}{12} \right]^{\frac{1}{2}} \tag{9}$$

where $c_{Ti}^{max}$ and $c_{Ti}^{min}$ are the maximum and minimum Ti concentrations at rutile saturation.

## 3. Results

### 3.1. Textures

As in the work of Tropper and Manning (2005), three types of rutile were present in the run products (Fig. 2). The starting crystals exhibited textures consistent with partial dissolution (Fig. 2b). During experiments the grains changed color from translucent, pale yellow to deep indigo–blue or black. This is due to trace reduction of $Ti^{4+}$ to $Ti^{3+}$, with charge-compensating $H^+$ substitution (Colasanti et al., 2007).

A second morphology, present in all run products, was minute acicular and/or dendritic rutile crystals that were largely restricted to the outer capsules (Fig. 2a). Their high nucleation density, growth morphology, and distribution indicate formation during quench.

In a few runs, a third rutile type was observed. In these cases, one to several grains of equant, subhedral, blue-to-black rutile were found in the outer capsule. The grains are tens to several hundred μm in their longest dimension. Similar crystals were noted in previous studies of calcite, rutile, and apatite (Caciagli and Manning, 2003; Tropper and Manning, 2005; Antignano and Manning, 2008). As in the previous work, these crystals are interpreted to have grown during experiments due to very small *T* gradients in the capsules, as supported by their low nucleation density and growth in the outer capsule. If not taken into account, such vapor-transport crystals (VTC) will lead to overestimation of solubility. This is illustrated in Fig. 3, which shows that where VTC grew, residual crystals progressively lost weight to give an *apparent* time-dependent increase in rutile solubility. In their investigation of calcite solubility, Caciagli and Manning (2003) showed that it was possible in some cases to collect all VTC and include them in the weighing to retrieve an accurate solubility determination; however, the crystals in the present study proved too small to collect and weigh, and all experiments in which VTC were observed were omitted from final solubility calculations (and, with the exception of experiments 800RA-8 and 9, from Table 1).

In experiments to which < 13 wt.% albite was added, the run products included residual corundum or paragonite, and minute silicate quench spherules. Paragonite was observed in runs at 700 °C, which were at 1.0 and 1.5 GPa (Table 1); in contrast, corundum formed at all *P* in the runs at 800 and 900 °C. These observations are consistent with experimental and thermodynamic constraints on paragonite and corundum stability in the system $Na_2O$–$Al_2O_3$–$SiO_2$–$H_2O$ (Chatterjee, 1970; Holland, 1979; Holland and Powell, 1998; Tropper and Manning, 2004). Both corundum

**Table 1**
Experimental results

| Experiment Number | $T$ (°C) | $P$ (GPa) | Duration (h) | $H_2O$ (mg) | Silicate[a] (mg) | Dissolved silicate[b] (wt.%) | Rutile in (mg) | Rutile out (mg) | Ti solubility (ppm) | Notes |
|---|---|---|---|---|---|---|---|---|---|---|
| *Rutile–$H_2O$* | | | | | | | | | | |
| R-4 | 700 | 1.0 | 8 | 41.884 | | | 1.0433 | 1.0429 | 6 (4) | |
| R-5 | 800 | 0.7 | 10 | 33.820 | | | 0.7741 | 0.7731 | 18 (5) | |
| R-1 | 800 | 1.0 | 10 | 42.120 | | | 0.7793 | 0.7785 | 11 (4) | |
| R-2 | 800 | 1.0 | 12 | 41.187 | | | 1.5638 | 1.5623 | 22 (4) | |
| R-3 | 800 | 1.0 | 12 | 37.132 | | | 1.6414 | 1.6398 | 26 (5) | |
| R-6 | 800 | 1.5 | 10 | 37.497 | | | 0.7734 | 0.7719 | 24 (5) | |
| R-7 | 800 | 2.0 | 10 | 32.138 | | | 2.7032 | 2.7017 | 28 (5) | |
| R-8 | 900 | 1.0 | 6 | 35.670 | | | 1.1195 | 1.1167 | 47 (5) | |
| R-9 | 950 | 1.0 | 8 | 33.949 | | | 1.0428 | 1.0392 | 64 (5) | |
| R-10 | 1000 | 1.0 | 10 | 34.444 | | | 1.0395 | 1.0327 | 118 (5) | |
| *Rutile–$H_2O$–$SiO_2$* | | | | | | | | | | |
| RQ-1 | 800 | 1.0 | 10 | 44.884 | 1.387 | 3.730 | 1.2308 | 1.2300 | 11 (4) | |
| RQ-2 | 800 | 1.0 | 10 | 33.820 | 3.009 | 6.88 | 1.6213 | 1.6198 | 25 (5) | +qz |
| *Rutile–$H_2O$–$NaAlSi_3O_8$* | | | | | | | | | | |
| 700RA-1 | 700 | 1.0 | 10 | 36.142 | 0.771 | 1.851–2.089 | 0.5310 | 0.5303 | 11 (5) | +pg |
| 700RA-2 | 700 | 1.0 | 10 | 36.322 | 1.626 | 3.808–4.285 | 1.5351 | 1.5335 | 25 (5) | +pg |
| 700RA-3 | 700 | 1.0 | 10 | 35.345 | 2.458 | 5.793–6.502 | 1.2355 | 1.2332 | 37 (5) | +pg |
| 700RA-5 | 700 | 1.0 | 10 | 31.456 | 2.616 | 6.850–7.678 | 0.9182 | 0.9156 | 46 (5) | +pg |
| 700RA-6 | 700 | 1.5 | 10 | 20.759 | 1.503 | 5.730–6.751 | 0.7773 | 0.7741 | 87 (8) | +pg |
| 800RA-15 | 800 | 0.7 | 10 | 34.321 | 2.382 | 6.199–6.490 | 1.9222 | 1.9176 | 75 (5) | +co |
| 800RA-4 | 800 | 1.0 | 10 | 40.924 | 0.911 | 2.009–2.178 | 2.5632 | 2.5594 | 54 (4) | +co |
| 800RA-5 | 800 | 1.0 | 8 | 36.263 | 1.247 | 3.070–3.324 | 1.0432 | 1.0391 | 66 (5) | +co |
| 800RA-6 | 800 | 1.0 | 10 | 32.421 | 1.123 | 3.092–3.348 | 1.2549 | 1.2515 | 61 (5) | +co |
| 800RA-7 | 800 | 1.0 | 12 | 36.223 | 1.273 | 3.136–3.395 | 1.2146 | 1.2102 | 70 (5) | +co |
| 800RA-8 | 800 | 1.0 | 16 | 31.233 | 1.107 | 3.162–3.423 | 1.6211 | 1.6129 | 152 (5) | +co, VTC |
| 800RA-9 | 800 | 1.0 | 14 | 26.576 | 0.964 | 3.233–3.500 | 1.0487 | 1.0443 | 96 (6) | +co, VTC |
| 800RA-10 | 800 | 1.0 | 12 | 41.026 | 2.810 | 5.935–6.410 | 3.3275 | 3.3206 | 95 (4) | +co |
| 800RA-11 | 800 | 1.0 | 12 | 35.623 | 2.603 | 6.306–6.810 | 2.1549 | 2.1494 | 86 (5) | +co |
| 800RA-12 | 800 | 1.0 | 10 | 36.959 | 3.568 | 8.166–8.804 | 2.3150 | 2.3061 | 132 (4) | +co |
| 800RA-14 | 800 | 1.0 | 8 | 36.080 | 5.254 | 11.827–12.711 | 0.7957 | 0.7835 | 178 (5) | +co |
| 800RA-1 | 800 | 1.2 | 10 | 30.211 | 2.243 | 6.284–6.911 | 0.7581 | 0.7514 | 124 (5) | +co |
| 800RA-2 | 800 | 1.5 | 10 | 28.896 | 2.045 | 5.871–6.609 | 0.7835 | 0.7752 | 161 (6) | +co |
| 800RA-3 | 800 | 2.0 | 10 | 30.450 | 2.151 | 5.705–6.598 | 1.3051 | 1.2930 | 223 (6) | +co |
| 900RA-4 | 900 | 1.0 | 10 | 28.848 | 0.560 | 1.757–1.904 | 0.7712 | 0.7642 | 143 (6) | +co |
| 900RA-5 | 900 | 1.0 | 10 | 34.108 | 1.601 | 4.144–4.483 | 2.1377 | 2.1296 | 136 (5) | +co |
| 900RA-6 | 900 | 1.0 | 10 | 35.429 | 2.437 | 5.958–6.436 | 2.3707 | 2.3569 | 219 (5) | +co |
| 900RA-7 | 900 | 1.0 | 6 | 29.912 | 4.325 | 11.753–12.633 | 1.0279 | 1.0067 | 373 (6) | +co |
| 900RA-8 | 900 | 1.0 | 6 | 39.280 | 7.717 | 15.323–16.420[c] | 1.2278 | 1.1931 | 445 (5) | +melt, co |
| 900RA-9 | 900 | 1.0 | 6 | 36.075 | 10.796 | 21.609–23.033[c] | 1.2026 | 1.1484 | 699 (7) | +melt, co |
| 900RA-10 | 900 | 1.0 | 6 | 27.625 | 15.996 | 34.784–36.670[c] | 1.1931 | 1.1195 | 1025 (13) | +melt, co |
| 900RA-1 | 900 | 1.5 | 6 | 35.450 | 2.469 | 5.783–6.511 | 1.0056 | 0.9885 | 271 (5) | +co |

Explanation: weights reported to three decimal places were determined on a Mettler M3 microbalance ($1\sigma$=2 μg), whereas those reported to four places were determined on a Mettler UMX2 ultramicrobalance ($1\sigma$=0.2 μg). Parenthetical numbers reflect $1\sigma$ uncertainty in final digits, based on propagation of weighing errors. Abbreviations: VTC, vapor-transport crystals; qz, quartz; pg, paragonite, co, corundum.

[a] Added silicate is quartz in $H_2O$–$SiO_2$ experiments and Amelia albite in $H_2O$–$NaAlSi_3O_8$ experiments (see text).

[b] Dissolved silicate concentration corrected for presence of residual phase indicated in "Notes" column, using solubility data from Manning (1994) for quartz or Anderson and Burnham (1983) and Antignano (2007) for paragonite or corundum. For $H_2O$–albite runs, dissolved silicate is given as a range between minimum, calculated from solubility data, and maximum, assuming congruent albite solubility (see text).

[c] Calculated silicate content is bulk composition of fluid+melt mixture.

and paragonite formed as mats of fine-grained hexagonal platelets in the outer capsule (Fig. 2c, d). Also present in the outer capsules of the relatively dilute albite experiments are micron-scale Na–Al–Si-bearing spherules. Textures indicate growth later than paragonite or corundum (Fig. 2c, d), which – when combined with their size, distribution, and location – indicate formation as quench "roe." Similar textures of $SiO_2$ spherules were observed in the two experiments to which quartz was added.

Three experiments were conducted at 900 °C and 1.0 GPa with nominal albite concentrations of >13 wt.%. In these runs, one or several large (>100 μm diameter) Na–Al–Si-bearing spheres were present with residual corundum (Fig. 4). These spheres are inferred to indicate saturation with hydrous silicate melt at run conditions.

### 3.2. Equilibrium

Initial experiments lasted 24 h, but formation of vapor-transport crystals indicated that shorter runs were required. Experimental results at 800 °C, 1 GPa, 3.3±0.2 wt.% albite indicated that 8–12 h runs gave constant solubility with time within error (Fig. 3). Accordingly, all experiments were conducted for 6–12 h. Equilibrium was approached from undersaturation in all cases.

### 3.3. Rutile–$H_2O$

Experimental results are given in Table 1 and Fig. 5. The data demonstrate that rutile solubility rises with increasing $P$ and $T$ (Fig. 5a). At 1.0 GPa and 700 °C, the measured weight change of 0.4 μg (experiment R-4, Table 1) is equivalent to $2\sigma$ of the weighing error, strictly below detection limits ($3\sigma$, or 9 ppm). At 800 °C, there is significant scatter, but the measurements agree at the $2\sigma$ level and are well above nominal detection limits. Determinations at 900, 950 and 1000 °C demonstrate isobaric increase in solubility with rising $T$. Experiments at 800 °C and 0.7 to 2.0 GPa suggest a linear increase in rutile solubility with $P$ (Fig. 5b).

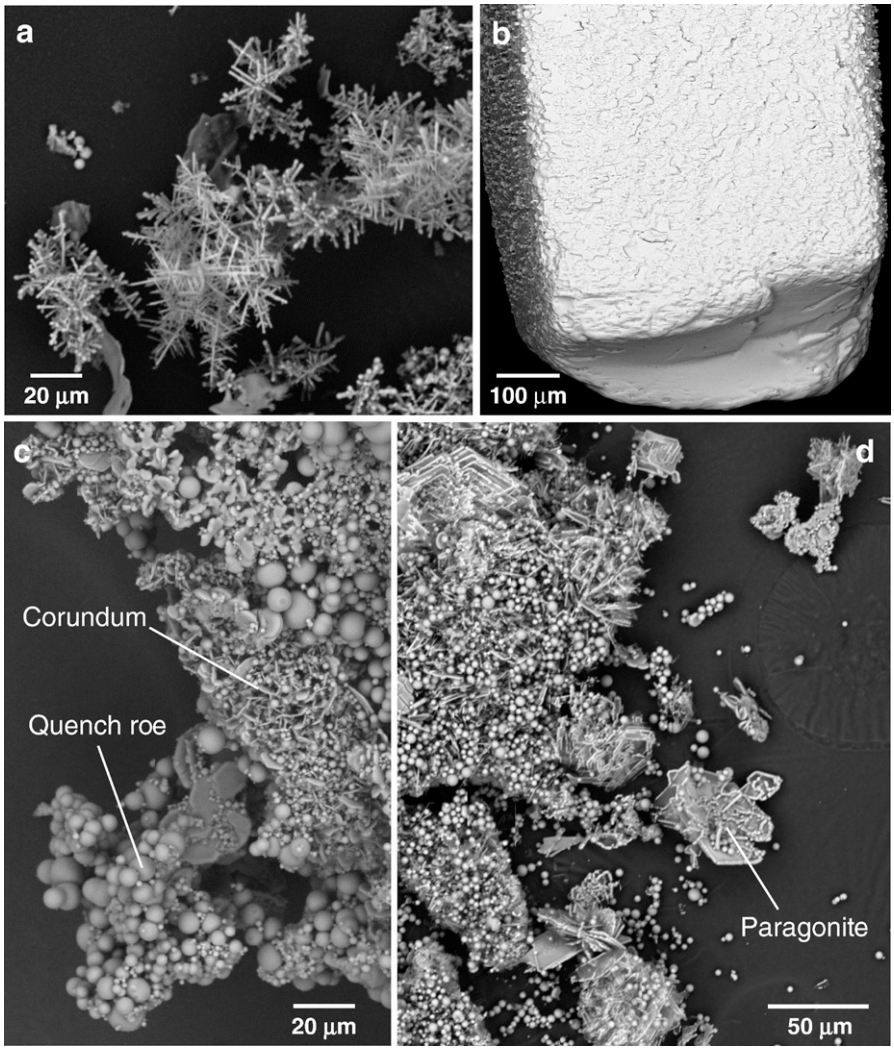


**Fig. 2.** SEM photomicrographs of run products from selected experiments. (a) Rutile needles from the outer capsule, which are interpreted to have formed upon quench. (b) Residual rutile crystal showing low-relief dissolution and reprecipitation textures. (c, d) Hexagonal corundum and paragonite crystals resulting from the incongruent dissolution of albite; spheres are quenched silicate solute ("quench roe").

Regression of the rutile solubility data at 800–1000 °C gives

$$\log c_{\mathrm{Ti}}^{\circ} = 6.173 - \frac{5425}{T} + \frac{178.4P}{T} \tag{10}$$

where $c_{\mathrm{Ti}}^{\circ}$ is in ppm Ti by weight, $T$ is in K, $P$ is in GPa, and normalized $\chi^2 = 2.1$. Extrapolation of Eq. (10) to 700 °C (Fig. 5a) gives the same value (6 ppm) as measured, suggesting that though this solubility measurement is below a nominal $3\sigma$ detection limit, it is nevertheless accurate.

### 3.4. Rutile–$H_2O$–$SiO_2$

Two experiments were conducted in $H_2O$–$SiO_2$ fluids at 800 °C and 1.0 GPa to assess possible $TiO_2$–$SiO_2$ solute interactions (Table 1). One experiment was conducted at quartz undersaturation (RQ-1, 3.73 wt.% $SiO_2$), and one at quartz saturation (RQ-2, 6.88 wt.% $SiO_2$, Manning, 1994). Measured Ti solubilities are indistinguishable from each other and from values determined in pure $H_2O$ at the $2\sigma$ level (Table 1). Thus, the addition of $SiO_2$ did not yield a measurable change in Ti solubility.

### 3.5. Rutile–$H_2O$–$NaAlSi_3O_8$

Results of experiments to which albite was added are shown in Figs. 6 and 7. At 1 GPa, the solubility of rutile increases linearly with dissolved silicate concentration at 700, 800 and 900 °C (Fig. 6). The slope of the isothermal change in rutile solubility with dissolved silicate becomes steeper as $T$ increases from 700 to 900 °C. At 900 °C, 1 GPa, experiments were extended beyond melt saturation at ~14± 1 wt.% dissolved silicate (Table 1, Fig. 6c). In these experiments, calculated dissolved silicate corresponds to the composition of the fluid+melt mixture (Table 1). Rutile solubility in the presence of a silicate melt increased linearly with increasing dissolved silicate, with no evident break in slope at melt saturation (Fig. 6c).

A series of experiments was also carried out within a narrow range of calculated dissolved silicate contents of 6.3±0.6 wt.% (Table 1). Fig. 7a shows that the solubility of rutile in 6.3 wt.% silicate solution at 1 GPa is higher at any $T$ than in pure $H_2O$. In addition, the logarithm of rutile solubility increases linearly in $1/T$ in both pure $H_2O$ and 6.3 wt.% silicate, with nearly identical slope. Rutile solubility in 6.3 wt.% silicate is higher still at 1.5 GPa; however, the temperature dependence is less strong (Fig. 7a). Experiments were also conducted on rutile solubility in 6.3 wt.% silicate solution at 800 °C as a function of $P$ (Fig. 7b). The data show that the solubility increase remains linear in log $P$, but the $P$ dependence is greater.

The roughly linear dependence of rutile solubility on dissolved silicate concentration at each $P$ and $T$ suggests an equation of the form

$$c_{\mathrm{Ti}} = c_{\mathrm{Ti}}^{\circ} + Bw_{\mathrm{s}} \tag{11}$$

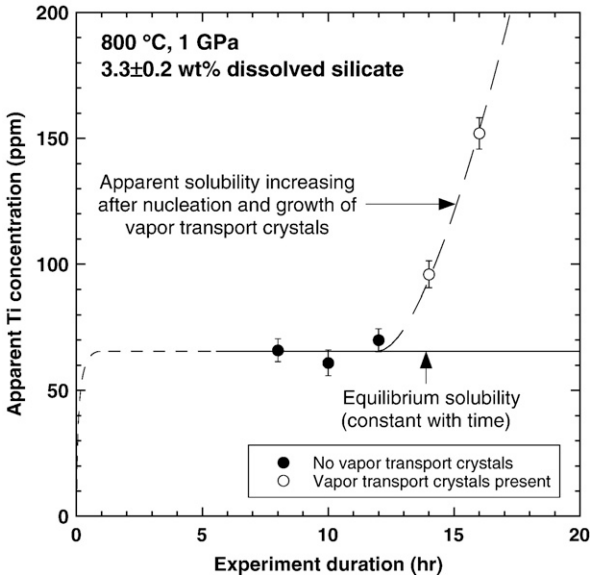


**Fig. 3.** Variation in apparent rutile solubility with time at 800 °C, 1 GPa, and 3.3 ± 0.2 wt.% dissolved Na–Al silicate. Filled circles show results of experiments in which no vapor-transport crystals (VTC) grew; open circles signify VTC-bearing experiments (1$\sigma$ error bars). Weight loss from the starting rutile crystal is constant with time at 8–12 h (solid line), but apparent solubility rises when VTC begin to grow in longer runs (long-dash line). The equilibrium solubility is therefore best determined in shorter runs. The approach to equilibrium (short dash lines) is probably tens of minutes to 1 h, based on results of Manning et al. (2008).

where $c_{Ti}$ is ppm Ti, $w_s$ is from Eq. (5) (in wt.%), and $B$ varies with $T$ and $P$. Regression analysis gave:

$$\log B = 6.512 - 1.665P - \frac{6224}{T} + \frac{2215P}{T} \quad (12)$$

where $T$ and $P$ are in K and GPa, respectively. Eqs. (11)–(12) reproduce the measurements to within an average of 9% (Figs. 6 and 7), with a maximum misfit of 46% for run 700RA-1 at 700 °C, 1 GPa and ~2 wt.% dissolved silicate. Eq. (12) has a one more term than Eq. (10). This term was necessary to minimize residuals and likely arises from the variation in the composition of dissolved silicate with $P$ and $T$.

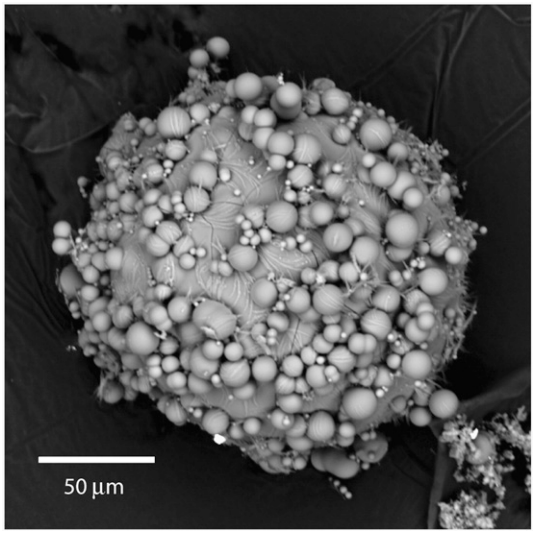


**Fig. 4.** SEM photomicrograph of a large, Na–Al-silicate glass sphere. The surface is partly coated with quench roe.

## 4. Discussion

### 4.1. Comparison to previous work

Our measured rutile solubilities in pure $H_2O$ are compared to previous results in Fig. 8. The study of Tropper and Manning (2005) used similar methods, but uncertainties were larger because of lower weighing precision. At 1 GPa, the two studies agree at 1000 °C at the 1$\sigma$ level, and Eq. (10) predicts solubility within 2$\sigma$ of the Tropper and Manning result at 1100 °C (Fig. 8a).

Ayers and Watson (1993) used hydrothermal piston-cylinder and weight-loss methods like Tropper and Manning (2005) and the present study; however, in agreement with Tropper and Manning (2005), we find substantially lower rutile solubility in $H_2O$ than did Ayers and Watson (1993) at all $P$ and $T$ investigated (Fig. 8). Tropper and Manning (2005) hypothesized that the difference is a result of misinterpretation of VTC as quench crystals by Ayers and Watson (1993). Antignano and Manning (2008) noted the same problem when comparing their results on fluorapatite solubility in $H_2O$ to those of

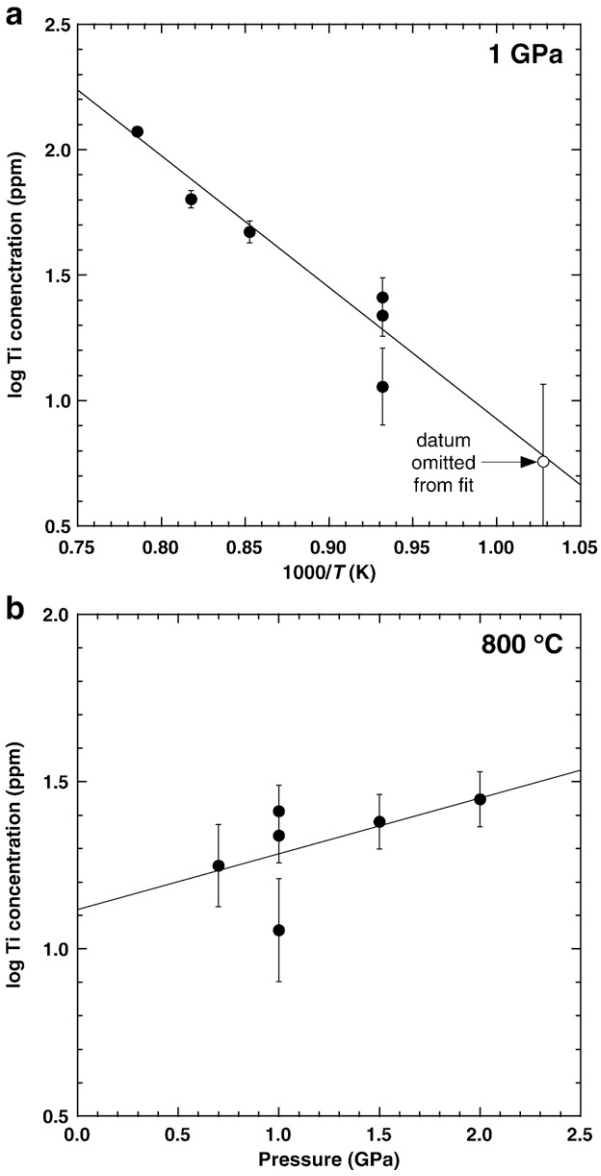


**Fig. 5.** Variation in rutile solubility in $H_2O$ with inverse temperature at 1 GPa (a) and with pressure at 800 °C (b). Solid line in both panels is the solubility calculated from Eq. (10). Error bars are 1$\sigma$. In (a), the measurement at 700 °C was omitted from the fitting because it is below 3$\sigma$ detection limits (see text).

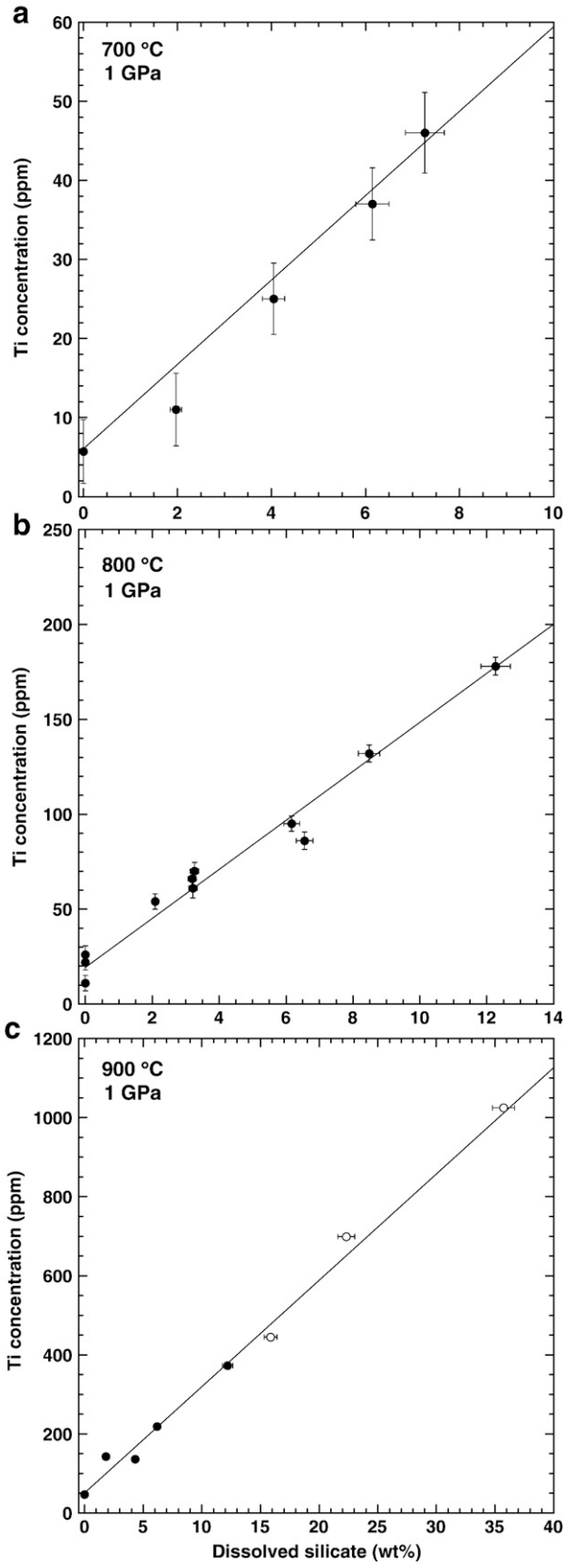


**Fig. 6.** Variation in rutile solubility with dissolved Na–Al silicate at 1 GPa and 700 °C (a), 800 °C (b), and 900 °C (c). Filled circles represent runs in which only a residual mineral (corundum or paragonite) was present; open symbols show runs with residual corundum that were saturated with hydrous Na–Al-silicate melt ($1\sigma$ error bars). In these experiments, calculated dissolved silicate corresponds to the composition of the fluid + melt mixture. Solid lines show solubilities predicted by Eqs. (11) and (12).

Ayers and Watson (1991). The hypothesis that misinterpretation of VTC as quench yields erroneously high solubilities is strongly supported by the results depicted in Fig. 3.

The solubility of rutile in $H_2O$ at a given $P$ and $T$ was found to be greater than that determined by Audétat and Keppler (2005) (Fig. 8). Our measured solubilities in $H_2O$–albite experiments are higher than those of Audétat and Keppler to an even greater degree (Fig. 9). Audétat and Keppler (2005) measured solubility by visually monitoring the disappearance and appearance of rutile crystals at high $P$ and $T$ in a hydrothermal diamond-anvil cell (HDAC). They suggested that the time needed for equilibrium was <1 s in the HDAC; however, Manning et al. (2008) found that equilibration times in the HDAC were longer (at least tens of minutes in Na–Al–Si-bearing fluids at similar $T$) and that, given sufficient time for equilibration, their HDAC results agreed with our piston-cylinder data. Overstepping of the $T$ of complete dissolution would result in apparent solubilities that were lower than equilibrium values. In addition, Audétat and Keppler (2005) discounted results from those albite–$H_2O$ experiments in which a hexagonal platy mineral (probably corundum) nucleated, but accepted those in which this phase did not grow; however, our results show that residual corundum should

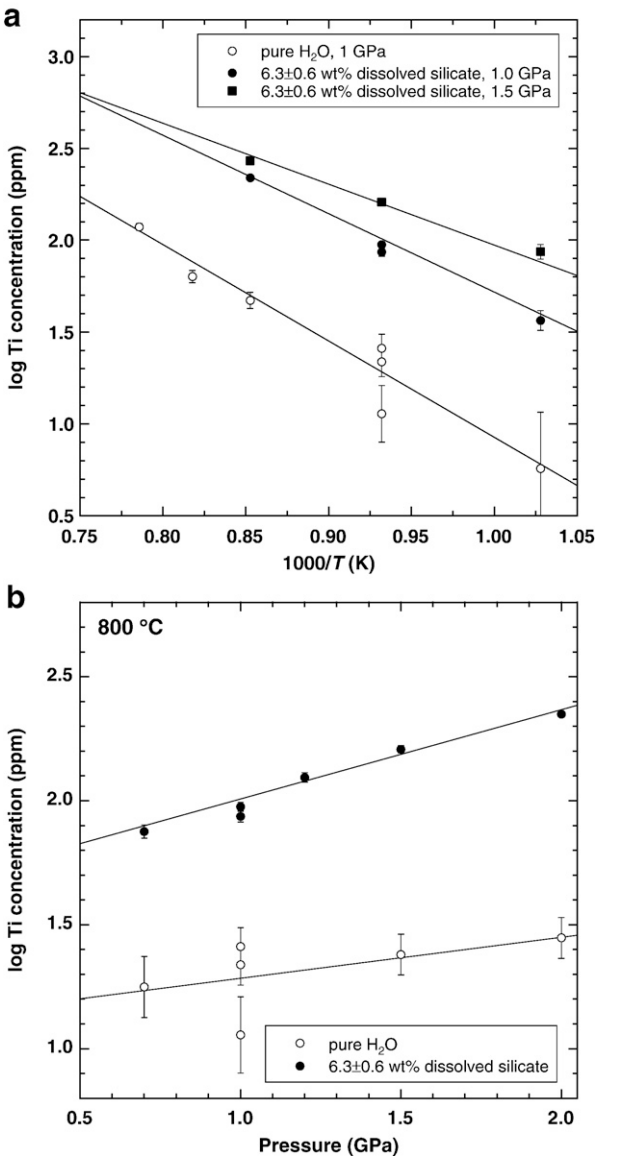


**Fig. 7.** Comparison of variation in rutile solubility with inverse temperature (a) and pressure at 800 °C (b) ($1\sigma$ error bars), at different fluid compositions. Solid lines show solubilities calculated from Eq. (10) (pure $H_2O$) and Eqs. (11) and (12) ($H_2O$–$NaAlSi_3O_8$ fluid).

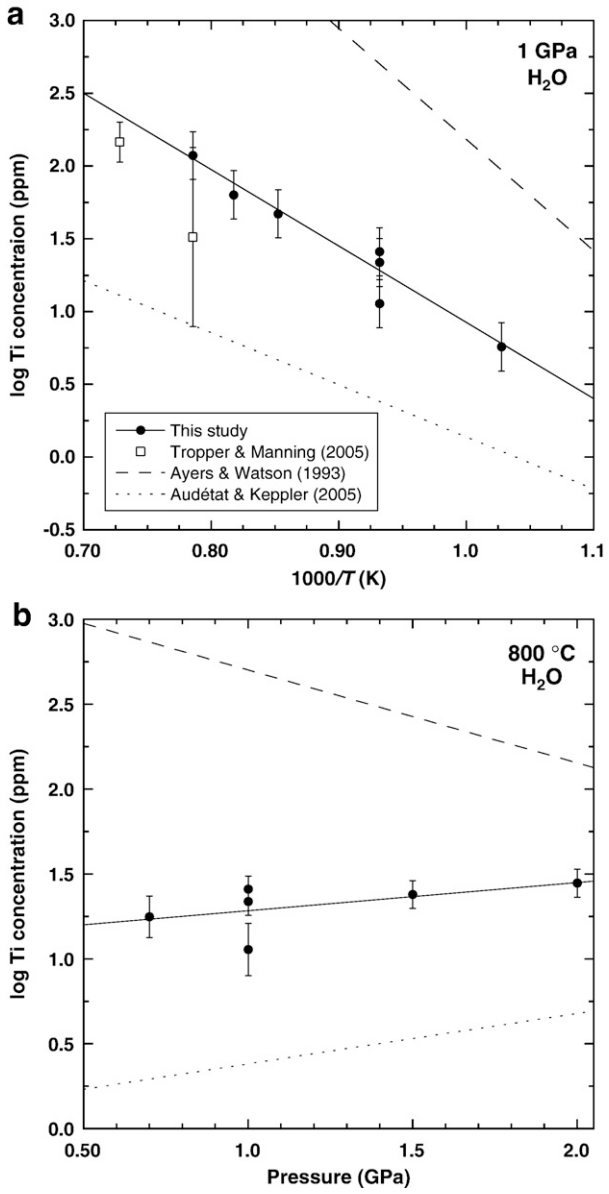


**Fig. 8.** Comparison of results of this study with previous work, depicted as a function of inverse temperature (a) and pressure (b) (1$\sigma$ error bars).

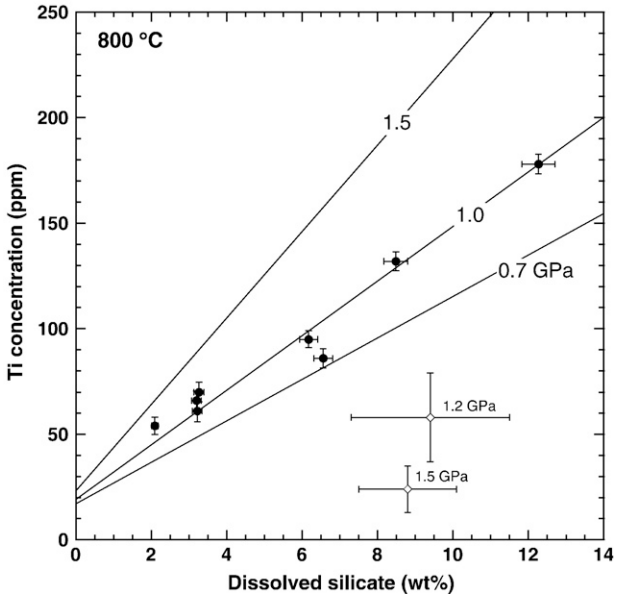


**Fig. 9.** Comparison of results of this study with those of Audétat and Keppler (2005) at 800 °C and varying dissolved silicate content. Filled circles show data from this work at 1 GPa (1$\sigma$ error bars); solid lines were calculated from Eqs. (11) and (12). Open diamonds show data of Audétat and Keppler (2005) at 1.2 and 1.5 GPa.

be present at equilibrium. Taken together, these observations suggest that the experiments of Audétat and Keppler (2005) were not fully equilibrated.

### 4.2. Thermodynamic properties of rutile dissolution

Rutile dissolution in $H_2O$ can be represented by the equilibrium

$$\underset{\text{rutile}}{TiO_2} = TiO_{2,aq}. \quad (13)$$

Adopting standard states for rutile and $TiO_{2,aq}$ of unit activity of the pure phase and of the hypothetical 1 m solution referenced to infinite dilution, respectively, and assuming unit activity coefficient for $TiO_{2,aq}$, the equilibrium constant for Eq. (13) ($K_{13}$) can be written

$$\ln K_{13} = \ln m_{TiO_{2,aq}} = \frac{\Delta S_r^\circ}{R} - \frac{\Delta H_r^\circ}{RT} - \frac{\Delta V_r^\circ}{RT}(P-1) \quad (14)$$

where $m_{TiO_{2,aq}}$ is dimensionless $TiO_2$ molality, and $\Delta S_r^\circ$, $\Delta H_r^\circ$, and $\Delta V_r^\circ$ are the standard molal entropy, enthalpy and volume changes of Eq. (13).

Values of the thermodynamic functions in Eq. (14) as derived from Eq. (10) are $\Delta S_r^\circ = 28.6$ J/mol K, $\Delta H_r^\circ = 104$ kJ/mol, and $\Delta V_r^\circ = -3.4$ cm$^3$/mol (Table 2). Consistent with the large discrepancies among the various rutile solubility studies, values determined from previous work vary widely. However, several considerations suggest that the current set of values is accurate. First, as noted by Tropper and Manning (2005), $\Delta V_r^\circ$ values for reactions like Eq. (13) and similar expressions for quartz, corundum or calcite dissolution (Manning, 1994; Caciagli and Manning, 2003; Tropper and Manning, 2007) are expected to be negative. All recent studies agree that $\Delta V_r^\circ$ of reaction 13 is about $-4.5 \pm 1.5$ cm$^3$/mol (Table 2), in contrast to the initial determination of Ayers and Watson (1993), which yielded positive $\Delta V_r^\circ$ of 11.3 cm$^3$/mol. Second, Eq. (13) is expected to be endothermic, which leads to increasing solubility with $T$ at high but constant $P$, as is the case for quartz, corundum and calcite. All studies have found positive $\Delta H_r^\circ$ (Table 2), though the magnitude differs by a factor of more than three. However, the highest $\Delta H_r^\circ$ values determined by Tropper and Manning (2005) and Ayers and Watson (1993) are likely a consequence of low precision and accuracy. The similarity in $\Delta H_r^\circ$ derived from the Audétat and Keppler (2005) and this work supports the interpretation that there was minor but fairly constant equilibrium overstep in the former study. Finally, the present investigation suggests that $\Delta S_r^\circ$ of reaction (13) is positive and similar to that of quartz = $SiO_{2,aq}$ (Walther and Helgeson, 1977).

Comparison of the isobaric variation in rutile solubility with $1/T$ in pure $H_2O$ vs. that in $H_2O$–$NaAlSi_3O_8$ suggests that $\Delta H_r^\circ$ is broadly similar, regardless of $P$ or the amount of dissolved silicate (Fig. 7a). However, the addition of dissolved Na–Al silicate leads to progressively greater $\Delta S_r^\circ$ at constant $P$ (Fig. 7a). In addition, the greater

**Table 2**
Thermodynamic properties of Eq. (13)

| Study | $\Delta S_r^\circ$ (J/mol K) | $\Delta H_r^\circ$ (kJ/mol) | $\Delta V_r^\circ$ (cm$^3$/mol) |
|---|---|---|---|
| Ayers and Watson (1993) | 98.4 | 135 | 11.3 |
| Tropper and Manning (2005) | 99.3 | 207 | −4.3 |
| Audétat and Keppler (2005) | −18.4 | 75 | −6.1 |
| This study | 28.6 | 104 | −3.4 |

Thermodynamic values for Tropper and Manning (2005) derived by refitting their data to $\log m TiO_{2,aq} = 5.187 - 1.080 \times 10^4/T + 2.270 \times 10^2 P/T$, with $T$ in K and $P$ in GPa.

positive dependence of rutile solubility on $P$ at 6.3 wt.% silicate relative to that in pure $H_2O$ indicates that $\Delta V_r^\circ$ becomes more negative with increasing dissolved Na–Al silicate.

### 4.3. Melt–vapor partitioning of Ti

Data from the present study allow semiquantitative assessment of the partitioning of Ti between a melt and a coexisting vapor phase at rutile saturation. $TiO_2$ contents in natural magmas were studied by Ryerson and Watson (1987), who gave a simple formula for estimating the $TiO_2$ concentration of rutile-saturated anhydrous melts as a function of $P$, $T$, and a melt compositional parameter, FM. Hayden and Watson (2007) updated this model for hydrous siliceous melts. They found that $TiO_2$ contents at 900 °C, 1 GPa, and rutile saturation in a peraluminous granite, were independent of $H_2O$ between 2.5 wt.% $H_2O$ and vapor saturation at ~12 wt.% $H_2O$. Their regression formula predicts that $H_2O$- and rutile-saturated Amelia albite melt (FM = 1.58) at 900 °C, 1 GPa, would contain 4200 ppm Ti. This can be compared to our results at the same $P$ and $T$. Neglecting minor incongruency and taking the $H_2O$ saturated composition on the albite–$H_2O$ join to be 86 wt.% albite (Burnham and Davis, 1974), linear extrapolation of Eq. (11) predicts 2400 ppm Ti in the melt. A linear extrapolation through the melt–vapor miscibility gap is crudely supported by the fact that rutile solubilities in our melt-saturated experiments at 900 °C, 1 GPa, lie on the regression line though they were not included in the derivation of the $B$ parameter (Eq. (12)). However, the coexisting melt composition must be slightly different than albite stoichiometry. With this uncertainty, it is therefore encouraging that the two studies agree as closely as they do. The good agreement motivated a similar comparison at 800 and 700 °C, which yielded 1100 ppm and 450 ppm (this study), as opposed to 1600 ppm and 500 ppm (Hayden and Watson, 2007), indicating even better agreement between the two studies at lower temperatures.

Because the present study yielded a constraint on the Ti content of the vapor phase at melt saturation at 900 °C, 1 GPa, the melt–vapor partition coefficient for Ti ($D_{Ti}$) can be estimated. The Hayden and Watson (2007) equation for $H_2O$–rutile-saturated Amelia albite melt yields 4200 ppm Ti, and Eq. (11) gives 427 ppm for the coexisting vapor phase (assuming 14 wt.% silicate), which yields $D_{Ti} = 9.9$.

A similar approach could be used to retrieve $D_{Ti}$ at 800 °C, 1 GPa, and at 700 °C, 1 GPa – which corresponds approximately to the $H_2O$-saturated solidus for albite (Goldsmith and Jenkins, 1985) – provided that the dissolved silicate in the vapor phase at melt saturation is known; however, our experiments at these temperatures were in all cases undersaturated with silicate melt. Thus, the solubilities at the highest nominal albite contents give only minimum values of 7.3 ± 0.4 wt.% and 12.3 ± 0.5 wt.% at 700 and 800 °C, respectively (Table 1). At 700 °C, the only other published constraint is from Shen and Keppler (1997) at 1.5 GPa, at which albite melt solubility is <10 wt.%. This is a maximum for 1 GPa because of the positive isothermal dependence of solubility on $P$. At 800 °C, a maximum solubility can be derived from the assumption that silicate solubility drops with decreasing $T$, which means that our 900 °C constraint of ~14 wt.% dissolved silicate at melt saturation must be a maximum for 800 °C. With these broad constraints, we calculate $D_{Ti}$ to be 8–11 at 700 °C and 8–9 at 800 °C.

The results indicate that, in this simple compositional system, $D_{Ti}$ is roughly constant at 9.5 ± 1.5 at 700–900 °C, 1 GPa. If applicable to more complex crustal magmas, this implies that significant magmatic Ti could be partitioned into the vapor phase upon saturation at these conditions. Thus, $H_2O$-rich magmatic fluids could be favorable metasomatic agents for Ti.

### 4.4. Mechanism of rutile solubility enhancement in $H_2O$–$NaAlSi_3O_8$

Our study reveals that there is a strong, roughly linear increase in rutile solubility with dissolved Na–Al silicate at a given $P$ and $T$ (Fig. 6), but that the presence of aqueous $SiO_2$ alone does not affect rutile solubility (Table 1). This implies that the presence of dissolved Na, Al, and Si together lead to complexing with Ti by providing coordination environments that are energetically more favorable than those in $H_2O$ or $H_2O$–$SiO_2$ fluids. Although our data do not provide direct constraints on the nature of specific complexes or solute interaction, they point to at least two possibilities. First, the excess Na indicated by incongruent albite dissolution could be used for complexing with Ti. In melts, $TiO_2$ solubility increases with (Na + K)/Al, suggesting formation of alkali-Ti complexes (Dickinson and Hess, 1985; Ryerson and Watson, 1987). Five-fold coordination of Ti is inferred to be abundant in melts in the system $Na_2O$–$TiO_2$–$SiO_2$ or $K_2O$–$TiO_2$–$SiO_2$ (Henderson and Fleet, 1995; Farges et al., 1996a,b; Farges, 1997; Henderson et al., 2003), and bond-valence considerations suggest that the Ti=O titanyl bond is a favorable site for alkali attachment (Romano et al., 2000). By analogy, penta-coordinated Ti in our Na–Al–Si-bearing aqueous solutions could be present as $NaOTi(OH)_4^-$ complexes.

A second possibility is suggested by the fact that the addition of Al to alkali-silicate melts leads to an increase in tetrahedral coordination of Ti due to competition by Al for charge-balancing alkali ions (Romano et al., 2000). In addition, recent evidence points to formation of Al-silicate, Na–Al-silicate, and K–Al-silicate clusters in aqueous solutions at high $P$ and $T$, with a significant fraction of tetrahedral Al and Si coordination (Manning, 2004, 2007; Newton and Manning, 2007, 2008; Mibe et al., 2008). Such clusters could plausibly accommodate $^{IV}$Ti substitution for $^{IV}$Al or $^{IV}$Si.

### 4.5. Geologic implications

To first order, increasing rutile solubility in $H_2O$ with rising $P$ and $T$ implies that deep, hot metasomatic environments are good candidates for Ti mobility. However, this study supports recent work (Audétat and Keppler, 2005; Tropper and Manning, 2005) which indicates that rutile solubility in $H_2O$ at high $P$ and $T$ is much lower than previously thought. Indeed, Eq. (10) predicts rutile solubility in $H_2O$ at 1000 °C, 2 GPa, of only 156 ppm. Raising Ti concentration sufficiently to generate Ti metasomatism at modest water–rock ratios or to produce rutile daughter crystals in fluid inclusions therefore requires a mechanism for enhancing Ti solubility that is more effective than $P$ and $T$ alone.

Prior work has suggested that extreme pH values or elevated F concentration could be responsible for Ti mobilization (Barsukova et al., 1979; Gieré, 1990; van Baalen, 1993). However, a problem with such models is that examples of Ti mobility are common in a wide range of bulk compositions, which are unlikely to buffer pore-fluid pH or $F^-$ activity at the requisite values. In contrast, because most crustal metamorphic and igneous rocks are rich in alkali feldspar components, it can be expected that dissolved Na, K, Al, and Si are abundant in aqueous fluids associated with crustal metamorphism and magma degassing, due to the high solubilities of albite and K feldspar in $H_2O$ at the $P$ and $T$ of the present study (Antignano (2008); Wohlers and Manning, 2007). Thus, our finding that rutile solubility increases with dissolved Na–Al silicate provides a simpler mechanism for enhancement of Ti solubility and promotion of Ti mobility. This conclusion is consistent with previous work on solute compositions in basalt–fluid and peridotite–fluid systems. In the basaltic system, Holloway (1971) found Ti concentrations of 240 ± 150 ppm in Si–Al–Na-rich fluids at 800–900 °C, 0.5–0.8 GPa, coexisting with magnetite. In addition, Schneider and Eggler (1986) determined that fluids equilibrated with amphibole or amphibole–peridotite were Si–Al–Na rich at 1.3–2.0 GPa and 750–900 °C, saturated with rutile and or titanite, and contained ~100 ppm Ti. In both studies, total solute contents were 1–2 wt.%, so Ti concentrations were higher than would be predicted by Eqs. (10)–(12), probably due to additional complexing with other dissolved constituents.

The conclusion that Ti solubility is enhanced by complexing with major rock-forming constituents such as alkalis, Al, and Si provides an

important insight into HFSE transport. To the extent that conditions causing enhancement of Ti solubility should also yield elevated solubility of allied HFSE elements, it can be expected that fluxing by alkali-Al silicate bearing aqueous solutions could provide a mechanism for the HFSE mobility that is observed in some metasomatic settings (Sorensen and Grossman, 1989; Philippot and Selverstone, 1991; Selverstone et al., 1992; Franz et al., 2001; Rubatto and Hermann, 2003; Jiang et al., 2005; John et al., 2008).

## 5. Conclusions

(1) Rutile solubility was measured by weight loss using hydrothermal piston-cylinder methods, taking special measures to avoid growth of vapor-transport crystals. We found that solubility in pure $H_2O$ at 700–1000 °C and 0.7–2.0 GPa increases with *P* and *T*. The results broadly agree with the imprecise data of Tropper and Manning (2005), but extend the measurements to lower *P* and *T*. Measured solubilities are significantly lower than were obtained by Ayers and Watson (1991); the discrepancy is interpreted to be a consequence of growth of vapor-transport crystals as quench in the earlier work. We obtained higher solubilities than Audétat and Keppler (2005). In this case the discrepancy appears to be due to small degrees of disequilibrium in their HDAC experiments (cf., Manning et al., 2008).

(2) The solubility of rutile in $H_2O$–$SiO_2$ fluids at 800 °C, 1 GPa, shows no measurable increase or decrease as a function of increasing dissolved $SiO_2$.

(3) The solubility of $H_2O$–$NaAlSi_3O_8$ fluids was complicated by incongruent dissolution of albite. Using previous work on albite solubility and a mass-balance calculation, we estimated fluid compositions and found that, at constant *P* and *T*, rutile solubility increases approximately linearly with added dissolved Na–Al silicate.

(4) The increase in rutile solubility with dissolved Na–Al silicate requires formation of a Ti complex involving Na, Al and or Si. Possibilities include five-coordinated $NaOTi(OH)_4^-$ and tetrahedrally coordinated Ti substituting for Al or Si in Na–Al–Si oligomeric clusters. Regardless of the solubility mechanism, the strong increase in Ti solubility with dissolved albite components demonstrates that Ti can be mobilized during fluid–rock interaction in high-*P* metasomatic environments.

## Acknowledgments

This project was part of the Ph.D. dissertation of the senior author. Partial support was provided by the University of California, Los Angeles, a Mineralogy and Petrology Research Grant from the Mineralogical Society of America, and National Science Foundation grants EAR-0337170 and EAR-0711521 to CEM. We thank R.C. Newton and P. Tropper for assistance and advice, and two anonymous reviewers for constructive comments on the manuscript.

## References

Agapova, G.F., Modnikov, I.S., Shmariovich, Y.M., 1989. Experimental study of the behavior of titanium in hot sulfide–carbonate solutions. International Geology Review 31, 424–430.

Anderson, G.M., Burnham, C.W., 1983. Feldspar solubility and the transport of aluminum under metamorphic conditions. American Journal of Science 283A, 283–297.

Antignano, A., 2008. Apatite and rutile solubility in water–sodium chloride and silicate-bearing fluids at high temperatures and pressures: Implications for metamorphic fluids. Unpublished Ph.D. Thesis, University of California, Los Angeles, 94 pp.

Antignano, A., Manning, C.E., 2008. Apatite solubility in $H_2O$ and $H_2O$–NaCl at 700 to 900 °C and 0.7 to 2.0 GPa. Chemical Geology 251, 112–119.

Audétat, A., Keppler, H., 2005. Solubility of rutile in subduction zone fluids, as determined by experiments in the hydrothermal diamond anvil cell. Earth and Planetary Science Letters 232, 393–402.

Ayers, J.C., Watson, E.B., 1991. Solubility of apatite, monazite, zircon, and rutile in supercritical aqueous fluids with implications for subduction zone geochemistry. Philosophical Transactions of the Royal Society of London Series A: Mathematical Physical and Engineering Sciences 335, 365–375.

Ayers, J.C., Watson, E.B., 1993. Rutile solubility and mobility in supercritical aqueous fluids. Contributions to Mineralogy and Petrology 114, 321–330.

Barsukova, M.L., Kuznetsov, V.A., Dorofeyeva, V.A., Khodakovskiy, L.I., 1979. Measurement of the solubility of rutile $TiO_2$ in fluoride solutions at elevated temperatures. Geochemistry International 16 (4), 41–49.

Bohlen, S.R., Wall, V.J., Boettcher, A.L., 1983. Experimental investigations and geological applications of equilibria in the system FeO–$TiO_2$–$Al_2O_3$–$SiO_2$–$H_2O$. American Mineralogist 68, 1049–1058.

Brenan, J.M., Shaw, H.F., Phinney, D.L., Ryerson, F.J., 1994. Rutile-aqueous fluid partitioning of Nb, Ta, Hf, Zr, U and Th — implications for high-field strength element depletions in island-arc basalts. Earth and Planetary Science Letters 128, 327–339.

Burnham, C.W., Davis, N.F., 1974. The role of $H_2O$ in silicate melts: II. Thermodynamic and phase relations in the system $NaAlSi_3O_8$–$H_2O$ to 10 kilobars, 700° to 1100 °C. American Journal of Science 274, 902–940.

Caciagli, N.C., Manning, C.E., 2003. The solubility of calcite in water at 6–16 kbar and 500–800 °C. Contributions to Mineralogy and Petrology 146, 275–285.

Chatterjee, N.D., 1970. Synthesis and upper stability of paragonite. Contributions to Mineralogy and Petrology 27, 244–257.

Colasanti, C.V., Johnson, E.A., Manning, C.E., 2007. Hydrogen solubility in synthetic rutile. Geochimica et Cosmochimica Acta 71 (Supplement), A181.

Corfu, F., Andrews, A.J., 1986. A U–Pb age for mineralized Nipissing Diabase, Gowganda, Ontario. Canadian Journal of Earth Science 23, 107–109.

Currie, K.L., 1968. On the solubility of albite in supercritical water in the range 400 to 600 °C and 750 to 3500 bars. American Journal of Science 266, 321–341.

Czamanske, G.K., Force, E.R., Moore, W.J., 1981. Some geologic and potential resources aspects of rutile in porphyry copper deposits. Economic Geology 76, 2240–2245.

Dickinson, J.E., Hess, P.C., 1985. Rutile solubility and titanium coordination in silicate melts. Geochimica et Cosmochimica Acta 49, 2289–2296.

Ernst, W.G., Liu, J., 1998. Experimental phase-equilibrium study of Al- and Ti-contents of calcic amphibole in MORB — a semiquantitative thermobarometer. American Mineralogist 83, 952–969.

Farges, F., 1997. Coordination of $Ti^{4+}$ in silicate glasses: a high-resolution XANES spectroscopy study at the Ti K edge. American Mineralogist 82, 36–43.

Farges, F., Brown, G.E., Navrotsky, A., Gan, H., Rehr, J.J., 1996a. Coordination chemistry of Ti(IV) in silicate glasses and melts: II. Glasses at ambient temperature and pressure. Geochimica et Cosmochimica Acta 60, 3039–3053.

Farges, F., Brown, G.E., Navrotsky, A., Gan, H., Rehr, J.J., 1996b. Coordination chemistry of Ti(IV) in silicate glasses and melts: III. Glasses and melts from ambient to high temperatures. Geochimica et Cosmochimica Acta 60, 3055–3065.

Floyd, P.A., Winchester, J.A., 1975. Magma type and tectonic setting discrimination using immobile elements. Earth and Planetary Science Letters 27, 211–218.

Floyd, P.A., Winchester, J.A., 1978. Identification and discrimination of altered and metamorphosed volcanic rocks using immobile elements. Chemical Geology 21, 291–306.

Foley, S.F., Barth, M.G., Jenner, G.A., 2000. Rutile/melt partition coefficients for trace elements and an assessment of the influence of rutile on the trace element characteristics of subduction zone magmas. Geochimica et Cosmochimica Acta 64, 933–938.

Force, E.R., 1980. The provenance of rutile. Journal of Sedimentary Petrology 50, 485–488.

Force, E.R., 1991. Geology of titanium-mineral deposits. Geological Society of America Special Paper 249. 112 pp.

Franz, L., Romer, R.L., Klemd, R., Schmid, R., Oberhänsli, R., Wagner, T., Dong, S., 2001. Eclogite-facies quartz veins within metabasites of the Dabie Shan (eastern China); pressure–temperature–time–deformation path, composition of the fluid phase and fluid flow during exhumation of high-pressure rocks. Contributions to Mineralogy and Petrology 141, 322–346.

Gao, J., Klemd, R., 2001. Primary fluids entrapped at blueschist to eclogite transition: evidence from the Tianshan meta-subduction complex in northwestern China. Contributions to Mineralogy and Petrology 142, 1–14.

Gao, J., John, T., Klemd, R., Xiong, X.M., 2007. Mobilization of Ti–Nb–Ta during subduction: evidence from rutile-bearing dehydration segregations and veins hosted in eclogite, Tianshan, NW China. Geochimica et Cosmochimica Acta 71, 4974–4996.

Gieré, R., 1990. Hydrothermal mobility of Ti, Zr, and REE: examples from the Bergell and Adamello contact aureoles (Italy). Terra Nova 2, 60–67.

Goldsmith, J.R., Jenkins, D.M., 1985. The hydrothermal melting of low and high albite. American Mineralogist 70, 924–933.

Hayden, L.A., Watson, E.B., 2007. Rutile saturation in hydrous siliceous melts and its bearing on Ti-thermometry of quartz and zircon. Earth and Planetary Science Letters 258, 561–568.

Henderson, G.S., Fleet, M.Y., 1995. The structure of Ti silicate glasses by micro-Raman spectroscopy. Canadian Mineralogist 33, 399–408.

Henderson, G.S., Liu, X.Y., Fleet, M.E., 2003. Titanium coordination in silicate glasses investigated using O K-edge X-ray absorption spectroscopy. Mineralogical Magazine 67, 597–607.

Holland, T.J.B., 1979. Experimental determination of the reaction paragonite = jadeite + kyanite + $H_2O$, and internally consistent thermodynamic data for part of the system $Na_2O$–$Al_2O_3$–$SiO_2$–$H_2O$, with applications to eclogites and blueschists. Contributions to Mineralogy and Petrology 68, 293–301.

Holland, T.J.B., Powell, R., 1998. An internally consistent thermodynamic data set for phases of petrological interest. Journal of Metamorphic Geology 16, 309–343.

Holloway, J.R., 1971. Composition of fluid phase solutes in a basalt–$H_2O$–$CO_2$ system. Geological Society of America Bulletin 82, 233–238.

Jiang, S.Y., Wang, R.C., Xu, X.S., Zhao, K.D., 2005. Mobility of high field strength elements (HFSE) in magmatic-, metamorphic-, and submarine-hydrothermal systems. Physics and Chemistry of the Earth 30, 1020–1029.
John, T., Klemd, R., Gao, J., Garbe-Schönberg, C.-D., 2008. Trace-element mobilization in slabs due to non steady-state fluid–rock interaction: constraints from an eclogite-facies transport vein in blueschist (Tianshan, China). Lithos 103, 1–24.
Klemme, S., Prowatke, S., Hametner, K., Gunther, D., 2005. Partitioning of trace elements between rutile and silicate melts: implications for subduction zones. Geochimica et Cosmochimica Acta 69, 2361–2371.
Kracek, F.C., Neuvonen, K.J., 1952. Thermochemistry of plagioclase and alkali feldspars. American Journal of Science 250, 293–318.
Manning, C.E., 1994. The solubility of quartz in $H_2O$ in the lower crust and upper mantle. Geochimica et Cosmochimica Acta 58, 4831–4839.
Manning, C.E., 2004. The chemistry of subduction-zone fluids. Earth and Planetary Science Letters 223, 1–16.
Manning, C.E., 2007. Solubility of corundum plus kyanite in $H_2O$ at 700 °C and 10 kbar: evidence for Al–Si complexing at high pressure and temperature. Geofluids 7, 258–269.
Manning, C.E., Boettcher, S.L., 1994. Rapid-quench hydrothermal experiments at mantle pressures and temperatures. American Mineralogist 79, 1153–1158.
Manning, C.E., Bohlen, S.R., 1991. The reaction titanite+kyanite=anorthite+rutile and titanite–rutile barometry in eclogites. Contributions to Mineralogy and Petrology 109, 1–9.
Manning, C.E., Wilke, M., Cauzid, J., 2008. Rutile solubility in albite–$H_2O$ and $Na_2Si_3O_7$–$H_2O$ at high temperatures and pressures by in-situ synchrotron radiation micro-XRF. Earth and Planetary Science Letters 272, 730–737.
Marsh, S.P., 1979. Rutile mineralization in the White Mountain andalusite deposit, California. U.S. Geological Survey Open-File Report 79-1622. 7 pp.
Mezger, K., Hanson, G.N., Bohlen, S.R., 1989. High-precision U–Pb ages of metamorphic rutile — application to the cooling history of high-grade terranes. Earth and Planetary Science Letters 96, 106–118.
Mezger, K., Rawnsley, C.M., Bohlen, S.R., Hanson, G.N., 1991. U–Pb garnet, sphene, monazite, and rutile ages: implications for the duration of high-grade metamorphism and cooling histories, Adirondack Mts., New York. Journal of Geology 99, 415–428.
Mibe, K., Chou, I.-M., Bassett, W.A., 2008. In situ Raman spectroscopic investigation of the structure of subduction-zone fluids. Journal of Geophysical Research 113, B04208.
Newton, R.C., Manning, C.E., 2007. Solubility of grossular, $Ca_3Al_2Si_3O_{12}$, in $H_2O$–NaCl solutions at 800 °C and 10 kbar, and the stability of garnet in the system $CaSiO_3$–$Al_2O_3$–$H_2O$–NaCl. Geochimica et Cosmochimica Acta 71, 5191–5202.
Newton, R.C., Manning, C.E., 2008. Solubility of corundum in the system $Al_2O_3$–$SiO_2$–$H_2O$–NaCl at 800 °C and 10 kbar. Chemical Geology 249, 250–261.
Pearce, J.A., Cann, J.R., 1971. Ophiolite origin investigated by discriminant analysis using Ti, Zr and Y. Earth and Planetary Science Letters 12, 339–349.
Pearce, J.A., Cann, J.R., 1973. Tectonic setting of basic volcanic rocks determined using trace element analyses. Earth and Planetary Science Letters 19, 290–300.
Pearce, J.A., Norrey, M.J., 1979. Petrogenetic implications of Ti, Zr, Y, and Nb variations in volcanic rocks. Contributions to Mineralogy and Petrology 69, 33–47.
Philippot, P., Selverstone, J., 1991. Trace-element-rich brines in eclogitic veins — implications for fluid composition and transport during subduction. Contributions to Mineralogy and Petrology 106, 417–430.
Romano, C., Paris, E., Poe, B.T., Giuli, G., Dingwell, D.B., Mottana, A., 2000. Effect of aluminum on Ti-coordination in silicate glasses: a XANES study. American Mineralogist 85, 108–117.
Rubatto, D., Hermann, J., 2003. Zircon formation during fluid circulation in eclogites (Monviso, Western Alps): implications for Zr and Hf budget in subduction zones. Geochimica et Cosmochimica Acta 67, 2173–2187.
Rudnick, R.L., Barth, M., Horn, I., McDonough, W.F., 2000. Rutile-bearing refractory eclogites: missing link between continents and depleted mantle. Science 287, 278–281.
Ryerson, F.J., Watson, E.B., 1987. Rutile saturation in magmas — implications for Ti–Nb–Ta depletion in island-arc basalts. Earth and Planetary Science Letters 86, 225–239.
Schneider, M.E., Eggler, D.H., 1986. Fluids in equilibrium with perdotite minerals: implications for mantle metasomatism. Geochimica et Cosmochimica Acta 50, 711–724.
Schuiling, R.D., Vink, B.W., 1967. Stability relations of some titanium-minerals (sphene, perovskite, rutile, anatase). Geochimica et Cosmochimica Acta 31, 2399–2411.
Selverstone, J., Morteani, G., Staude, J.-M., 1991. Fluid channeling during ductile shearing: transformation of granodiorite into aluminous schist in the Tauern Window, Eastern Alps. Journal of Metamorphic Geology 9, 419–432.
Selverstone, J., Franz, G., Thomas, S., Getty, S., 1992. Fluid variability in 2 GPa eclogites as an indicator of fluid behaviour during subduction. Contributions to Mineralogy and Petrology 112, 341–357.
Shen, A.H., Keppler, H., 1997. Direct observation of complete miscibility in the albite–$H_2O$ system. Nature 385, 710–712.
Shmulovich, K.I., Graham, C., Yardley, B., 2001. Quartz, albite and diopside solubilities in $H_2O$–NaCl and $H_2O$–$CO_2$ fluids at 0.5–0.9 GPa. Contributions to Mineralogy and Petrology 141, 95–108.
Sorensen, S.S., Grossman, J.N., 1989. Enrichment of trace-elements in garnet amphibolites from a paleo-subduction zone — Catalina Schist, Southern-California. Geochimica et Cosmochimica Acta 53, 3155–3177.
Stalder, R., Foley, S.F., Brey, G.P., Horn, I., 1998. Mineral-aqueous fluid partitioning of trace elements at 900 GPa to 5.7 GPa: new experimental data set for garnet, clinopyroxene and rutile and implications for mantle metasomatism. Geochimica et Cosmochimica Acta 62, 1781–1801.
Stalder, R., Ulmer, P., Thompson, A.B., Günther, D., 2000. Experimental approach to constrain second critical end points in fluid/silicate systems: near-solidus fluids and melts in the system albite–$H_2O$. American Mineralogist 85, 68–77.
Tomkins, H.A., Powell, R., Ellis, D.J., 2007. The pressure dependence of the zirconium-in-rutile thermometer. Journal of Metamorphic Geology 25, 703–713.
Triebold, S., von Eynattena, H., Luvizotto, G.L., Zack, T., 2007. Deducing source rock lithology from detrital rutile geochemistry: an example from the Erzgebirge, Germany. Chemical Geology 244, 421–436.
Tropper, P., Manning, C.E., 2004. Paragonite stability at 700 °C in the presence of $H_2O$–NaCl fluids: constraints on $H_2O$ activity and implications for high pressure metamorphism. Contributions to Mineralogy and Petrology 147, 740–749.
Tropper, P., Manning, C.E., 2005. Very low solubility of rutile in $H_2O$ at high pressure and temperature, and its implications for Ti mobility in subduction zones. American Mineralogist 90, 502–505.
Tropper, P., Manning, C.E., 2007. The solubility of corundum in $H_2O$ at high pressure and temperature and its implications for Al mobility in the deep crust and upper mantle. Chemical Geology 240, 54–60.
Tropper, P., Manning, C.E., in press. Titanite–rutile thermobarometry in ultra-high-pressure metamorphic rocks: the influence of titanite activity models on phase equilibrium calculations. Chemical Geology. doi:10.1016/j.chemgeo.2008.03.010.
van Baalen, M.R., 1993. Titanium mobility in metamorphic systems: a review. Chemical Geology 110, 233–249.
Walther, J.V., Helgeson, H.C., 1977. Calculation of the thermodynamic properties of aqueous silica and the solubility of quartz and its polymorphs at high pressures and temperatures. American Journal of Science 277, 1315–1351.
Watson, E.B., Harrison, T.M., 2005. Zircon thermometer reveals minimum melting conditions on earliest Earth. Science 308, 841–844.
Watson, E.B., Wark, D.A., Thomas, J.B., 2006. Crystallization thermometers for zircon and rutile. Contributions to Mineralogy and Petrology 151, 413–433.
Wohlers, A., Manning, C.E., 2007. Model crustal fluids at high *P* and *T*: Implications for aluminum transport. Geochimica et Cosmochimica Acta 71 (15), A1123 Supplement.
Zack, T., Luvizottow, G.L., 2006. Application of rutile thermometry to eclogites. Mineralogy and Petrology 88, 69–85.
Zack, T., Kronz, A., Foley, S.F., Rivers, T., 2002. Trace element abundances in rutiles from eclogites and associated garnet mica schists. Chemical Geology 184, 97–122.
Zack, T., Moraes, R., Kronz, A., 2004a. Temperature dependence of Zr in rutile: empirical calibration of a rutile thermometer. Contributions to Mineralogy and Petrology 148, 471–488.
Zack, T., Eynatten, H., von Kronz, A., 2004b. Rutile geochemistry and its potential use in quantitative provenance studies. Sedimentary Geology 171, 37–58.